nature materials

SUPPLEMENTARY INFORMATION

DOI: 10.1038/NMAT3723

Persistence of magnetic excitations in $La_{2-x}Sr_xCuO_4$ from the undoped insulator to the heavily overdoped non-superconducting metal

Here we provide a diagram of the scattering geometry, details of the film growth and characterization, further explanation of the fitting procedure, plots of the x-ray absorption spectra for the samples, a discussion of the RIXS intensities and spin wave calculations of the magnetic spectral weight in La_2CuO_4.

I. DIAGRAM OF THE SCATTERING GEOMETRY

Figure 1 shows the scattering geometry used in the experiment. During the experiment the sample is rotated about the vertical axis b in the direction of increasing θ_i to increase the projection of $\boldsymbol{Q}$ onto $\boldsymbol{Q}_\parallel$, following the equation $Q_\parallel = 2|\boldsymbol{k}_i|\sin(2\theta/2)\sin(\delta)$.

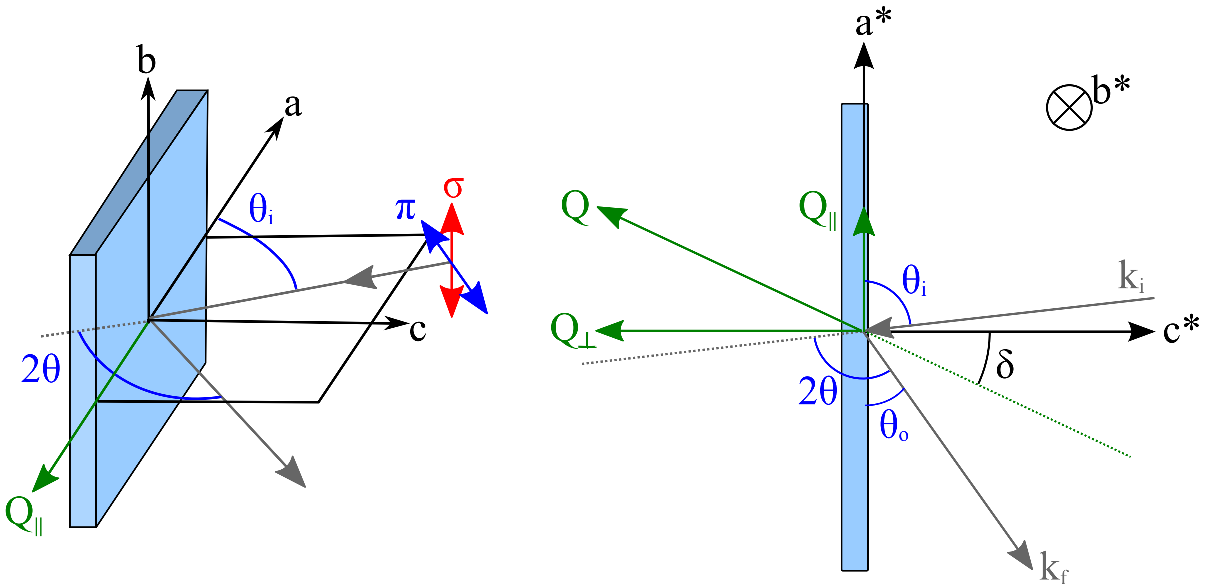

FIG. 1. The scattering geometry used in the experiment showing the definitions of the different angles and vectors used. The left panel is a 3D representation, and the right panel shows the a^*-c^* plane. a, b and c (a^*, b^* and c^*) are the direct (reciprocal) lattice vectors. $\boldsymbol{k}_i$ and $\boldsymbol{k}_f$ are the initial and final scattering vectors of the x-rays. $2\theta = 130°$ is the angle between $\boldsymbol{k}_i$ and $\boldsymbol{k}_f$. The angle between the sample surface and $\boldsymbol{k}_i$ is denoted θ_i; similarly θ_o is the angle between the sample surface and $\boldsymbol{k}_f$. $\boldsymbol{Q}$ is the total momentum transfer, which is resolved into $Q_\parallel$, parallel to a^*, and $Q_\perp$, parallel to c^*.

II. FILM SYNTHESIS AND CHARACTERIZATION

A. ALL-MBE system

For film synthesis, we used an advanced atomic-layer-by-layer molecular beam epitaxy (ALL MBE) system designed for growth of multilayers and heterostructures made of complex oxides.[1] This technique allows reproducible fabrication of atomically smooth films of cuprates with control of the stoichiometry at the 1% level. We have demonstrated the capability to synthesize films in which HTS superfluid is confined to a single CuO_2 plane, and yet the critical temperature (T_c) is comparable to that in optimally doped bulk $La_{2-x}Sr_xCuO_4$ single crystals.[2–4]

The growth kinetics was controlled by source opening and closing, effectuated by means of pneumatically actuated linear-motion shutters. The deposition rates were monitored and controlled in real time using an Atomic Absorption Spectroscopy system.[1] The absolute rates were calibrated before each growth using a quartz crystal balance, which was in turn calibrated occasionally by various *ex-situ* techniques (Rutherford backscattering, grazing-angle X-ray reflectance oscillations, X-ray diffraction finite-thickness fringes, film thickness measurements by Atomic Force Microscopy, etc.).

B. Film growth

The films under study were deposited onto $10 \times 10 \times 1$ mm^3 $LaSrAlO_4$ (LSAO) single-crystals. These LSAO substrates were polished to epitaxial smoothness with the surface perpendicular to the [001] crystallographic axis. The substrates were cleaned by ultrasonic agitation in acetone and isopropyl alcohol and annealed at elevated temperature (e.g. 950°C, 1 hour). The surface quality of every substrate was inspected before growth by atomic force microscopy (AFM).

During the film growth the nominal substrate temperature (the pyrometer reading) was kept at $T_s \approx 680°\mathrm{C}$. The film synthesis took place in an atmosphere of essentially pure ozone, at $p \approx 6 \times 10^{-6}$ Torr. The growth rate was kept very low; one 0.5 unit cell (UC) thick layer was deposited in about 100 seconds and this was followed by a 20 second pause to allow for surface relaxation, resulting in the overall growth rate of 0.05 Å/sec.

After growth, the La_2CuO_4 and $La_{1.9}Sr_{0.1}CuO_4$ films were cooled in ozone down to $T_s = 300$ °C after which the ozone supply was closed, the films annealed for 30 minutes in high vacuum to remove any interstitial oxygen, and then cooled down to room temperature. We have verified in numerous independent experiments that this procedure efficiently removes interstitial oxygen from undoped and underdoped LSCO films. Optimally doped and overdoped LSCO films were cooled in ozone down to $T_s < 100$ °C. The $x = 0.00$, $x = 0.16$ and $x = 0.40$ films were 40 unit cells (53 nm) thick and the $x = 0.11$ and $x = 0.26$ films were 75 units cells (99 nm) thick.

C. Reflection high-energy-electron-diffraction (RHEED)

Reflection High Energy Electron Diffraction (RHEED) was used to monitor the quality of film growth in real time. RHEED provides atomic-scale information about the smoothness of the surface; in particular, it can reveal nucleation of secondary-phase precipitates that may emerge because of inaccurate stoichiometry or inadequate thermodynamic parameters during growth. A well-established signature of atomically smooth layer-by-layer growth is the oscillations of the intensity of the specular spot in time. The maxima of reflectance are reached each time an atomic or molecular layer is completed, and the surface becomes atomically flat.

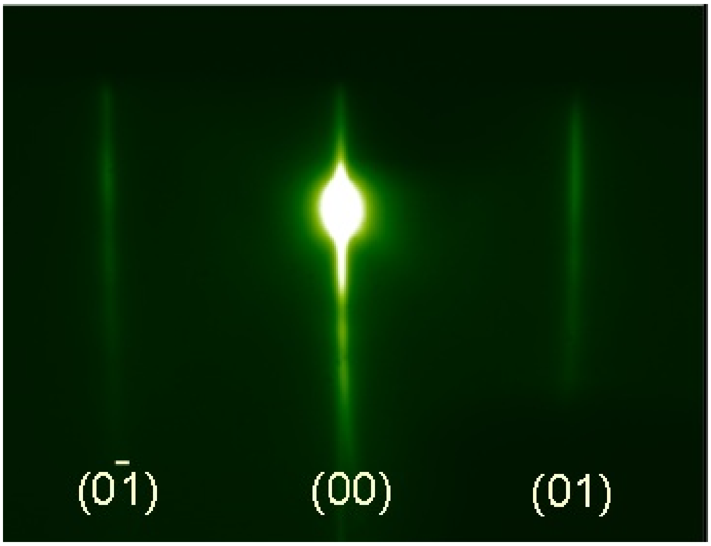

FIG. 2. RHEED pattern recorded at the end of growth of a 40 UC thick $La_{1.60}Sr_{0.40}CuO_4$ film on a single-crystal $LaSrAlO_4$ substrate. The electron beam is impinging along the [100] direction. The distance between the main streaks corresponds to the inverse of the in-plane lattice constant ($a_0 = 3.8$ Å) of $La_{1.60}Sr_{0.40}CuO_4$. The very strong specular reflection is indicative of an atomically flat surface.

In Fig. 2, we show the RHEED pattern obtained from the surface of a 40 UC thick $La_{1.60}Sr_{0.40}CuO_4$ film. Note that such extremely overdoped LSCO films are the most difficult to grow single-phase; indeed, all other films studied here showed similar or even better RHEED patterns. The intense specular reflection seen in Fig. 2 indicates that the surface is very flat. Long diffraction streaks indicate high surface crystallinity (with some terracing that originates from a slight miscut of the substrate). Secondary phase precipitates, if present, form as small grains on the sample surface and result in additional "transmission spots" in the RHEED image. The absence of such spots in Fig. 2 indicates the absence of secondary-phase precipitates in this sample.

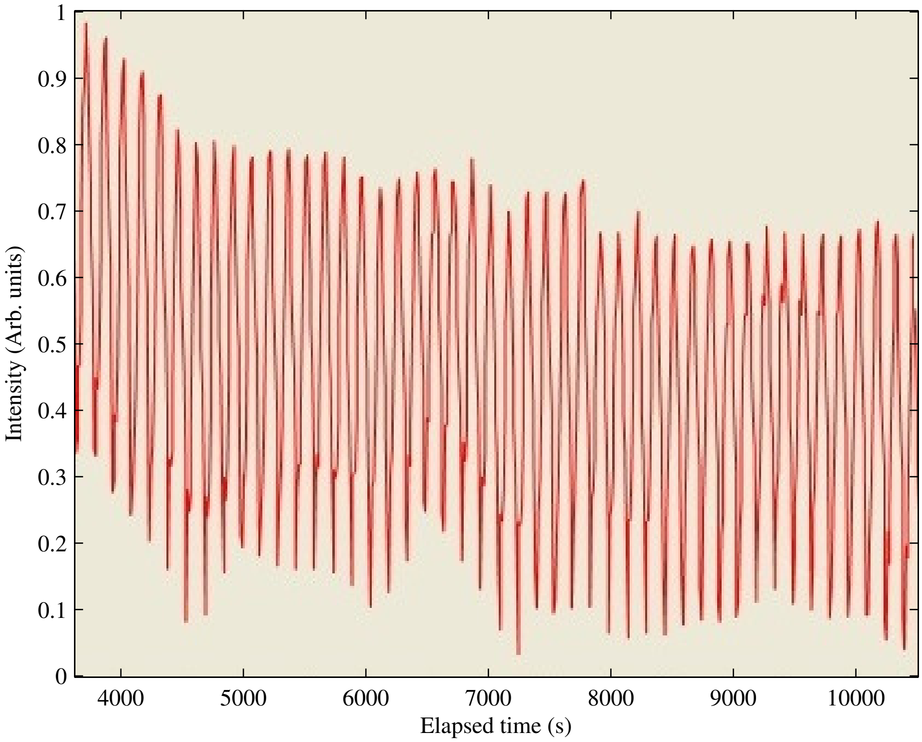

FIG. 3. The oscillations in the intensity of the specular reflection as a function of time recorded during growth of the same film as in Fig. 2. The RHEED oscillations originate from periodic roughening and smoothening of the surface; the intensity reaches a maximum each time a molecular layer is completed and the surface becomes atomically smooth.

In Fig. 3, we show the intensity of the specular reflection spot plotted as a function of time, for the same $La_{1.60}Sr_{0.40}CuO_4$ film. The graph shows pronounced RHEED oscillations; the maxima are reached each time when a molecular (0.5 UC thick) layer is completed, and the surface gets atomically flat. Similar RHEED oscillations were observed and recorded during growth of all the other $La_{2-x}Sr_xCuO_4$ films studied in this work.

D. Atomic Force Microscopy (AFM)

The films' quality was double-checked after the growth (*ex situ*) by Atomic Force Microscopy (AFM). We used a Veeco MultiMode system equipped with a Nanoscope III controller and an

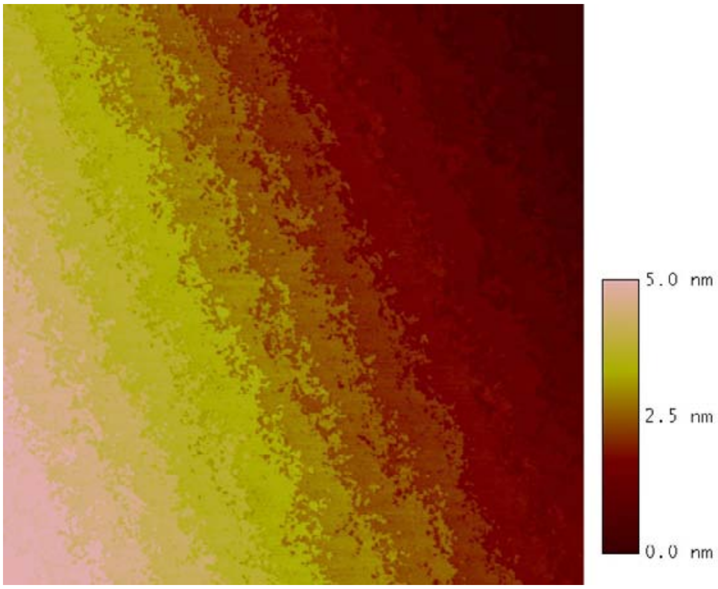

FIG. 4. Atomic-force microscope (AFM) image of the surface of a $LaSrAlO_4$ substrate. The rms surface roughness, over the AFM scan area of 5 × 5 μm, is less than 2 Å. This includes the terraces separated by 0.5 UC tall steps, which originate from a slight miscut of the substrate.

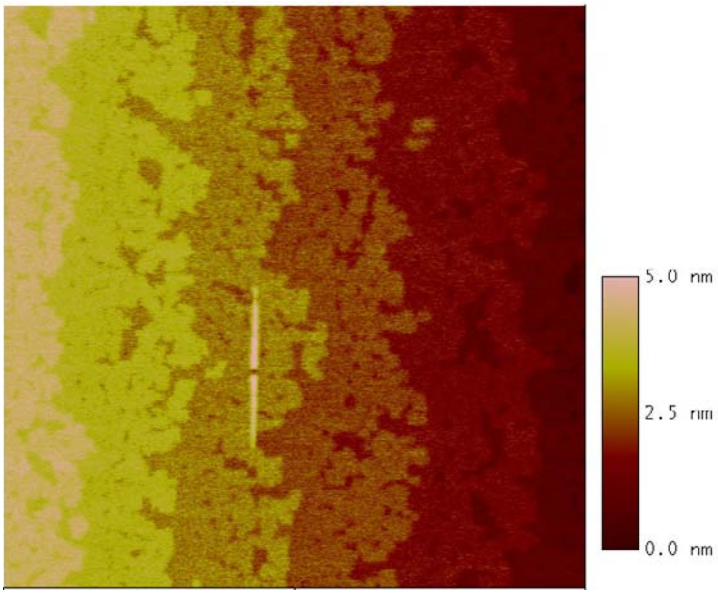

FIG. 5. AFM image of the surface of $La_{1.6}Sr_{0.40}CuO_4$ film deposited on LSAO substrate. The films thickness is 40 unit cell (UC), i.e., 530 Å. The rms roughness, over the scan area of 5 × 5 μm, is less than 3 Å. The terraces are separated by 0.5 UC tall steps, which originate from substrate miscut.

Extender module. Topography scans were done in tapping mode at a resonant frequency of 300 kHz, using OTESPA tips (tip radius 7-10 nm).

While the LSAO substrates were supposed to be polished with the surface perpendicular to the [001] crystallographic direction, in reality the orientation is usually slightly off, with a typical miscut of about 0.1°. Once a substrate is cleaned, as described in Section II B , AFM images of its surface show well-defined terraces with 0.5 UC (0.63 nm) tall steps. The clean LSAO substrates that we use in MBE growth typically have rms roughness below 2 Å. A typical AFM image of an LSAO substrate is shown in Fig. 4.

AFM images of our $La_{2-x}Sr_xCuO_4$ films grown on LSAO substrates exhibit rms surface roughness below 0.5 nm and absence of any secondary-phase precipitates, grains, or grain boundaries. In Fig. 5, we show an AFM image taken from the same $La_{1.60}Sr_{0.40}CuO_4$ film as in Figs. 2 and 3. The measured rms surface roughness is less than 0.3 nm.

E. X-ray diffraction (XRD)

After growth, every film was studied by X-Ray diffraction (XRD), by means of PANalytical X'Pert Pro MRD 4-circle diffractometer, using X-rays of wavelength $\lambda_{\mathrm{Cu\ K}-\alpha 1} = 1.5406$ Å. The scan geometry was aligned to the (004) Bragg peak of the $LaSrAlO_4$ substrate, which corresponds to planes parallel to the surface. A $2\theta - \omega$ scan between 25° – 30°, as shown in Fig. 6, revealed a sharp (004) $La_{2-x}Sr_xCuO_4$ Bragg peak, and from its positions we calculated the lattice constant for each sample using the known value (12.6357 Å) of the lattice constant of the LSAO substrate as the reference.

Sample	Doping x	Thickness (nm)	Lattice constant c_0 (Å)
#471	0	49 ± 2	13.165 ± 0.01
#943	0.11	85 ± 2	13.222 ± 0.01
#966	0.16	97 ± 3	13.284 ± 0.01
#1051	0.26	52 ± 3	13.279 ± 0.01
#1489	0.40	54 ± 3	13.276 ± 0.01
LSAO substrate	...	10^6	12.636 ± 0.001

TABLE I. X-ray diffraction data for the five $La_{2-x}Sr_xCuO_4$ films studied in this work. The doping levels are indicated. The film thickness is estimated from the spacing of finite-thickness fringes. The c-axis lattice constant is determined from the (004) Bragg peak, calibrated against the known value of the lattice constant of LSAO substrate.

The X-ray data (Fig. 6) confirm excellent film crystallinity and absence of any unwanted phases. The c axis lattice constant values (see Table I) are consistent with the literature data as well as with

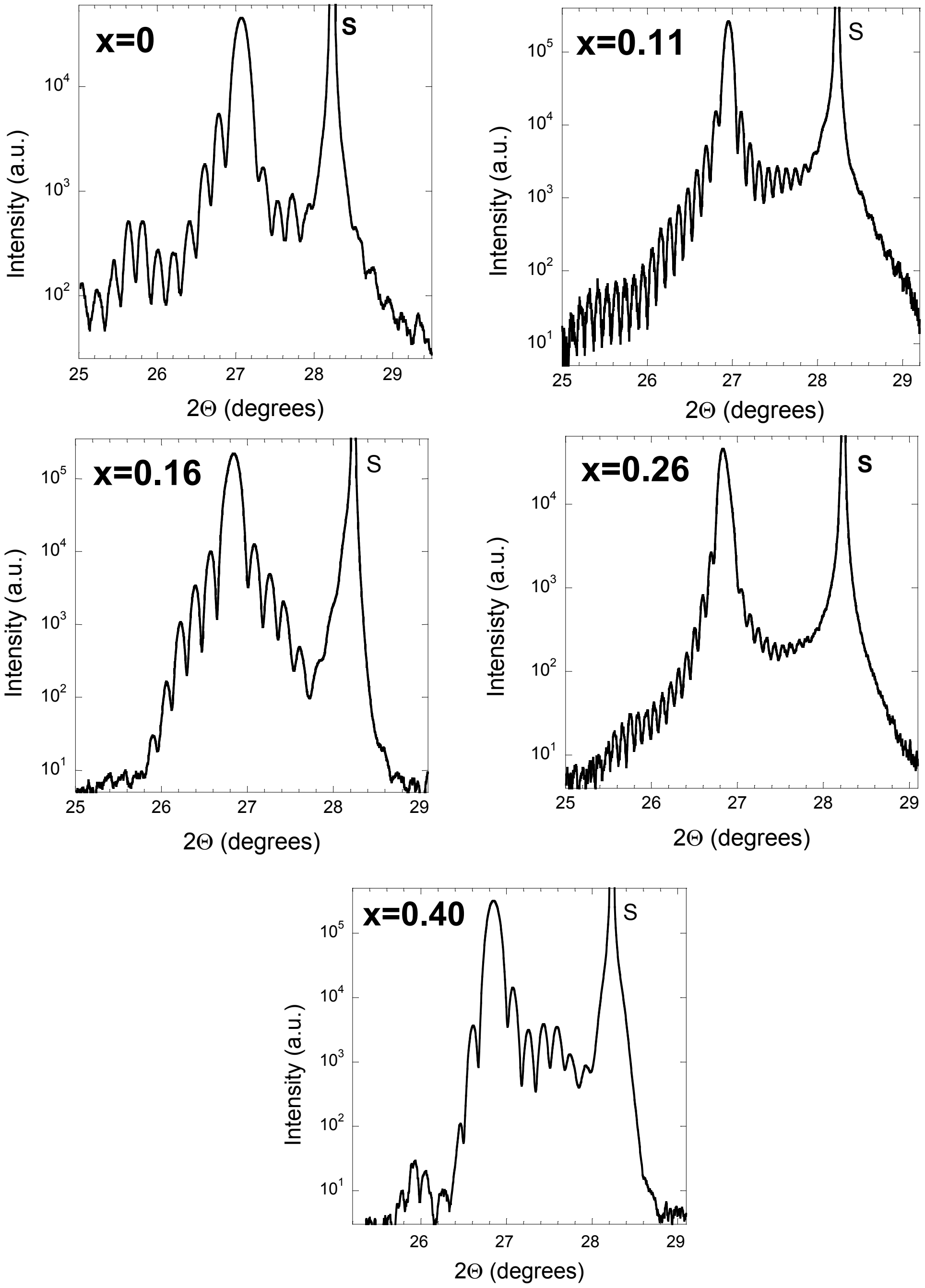

FIG. 6. X-ray diffraction data for the $La_{2-x}Sr_xCuO_4$ films studied here. The doping levels are as indicated in each panel. The label "S" indicates the (004) Bragg peak of the single-crystal $LaSrAlO_4$ substrate. The main (004) peak of the film is accompanied by finite-thickness oscillations, indicative of high crystallinity and atomically smooth surfaces and interfaces.

our numerous measurements on other $La_{2-x}Sr_xCuO_4$ films. Pronounced finite-thickness oscillations provide additional evidence of atomically smooth surfaces and interfaces. From the spacing between these satellite fringes one could get an estimate of the films thickness; the values are listed in Table I and they are reasonably close to the targeted film thickness.

F. Mutual inductance measurements

Magnetic susceptibility was measured using a two-coil mutual inductance technique in transmission geometry[5–8] in which the sample is sandwiched between the drive and pick-up coils. Since the mutual inductance measurements do not require any photolithographic processing, contamination of the LSCO film by photo-resist is avoided. The measurements were done in helium exchange gas to ensure a good temperature control. Magnetic susceptibility was typically measured while the sample was cooled down slowly at a rate of 0.1 K/min. An AC signal with amplitude of 5 μA and frequency ν = 10 kHz was applied to the driving coil and the induced voltage in the pickup coil was measured by a lock-in amplifier. The average radius of the coils is 0.9 mm.

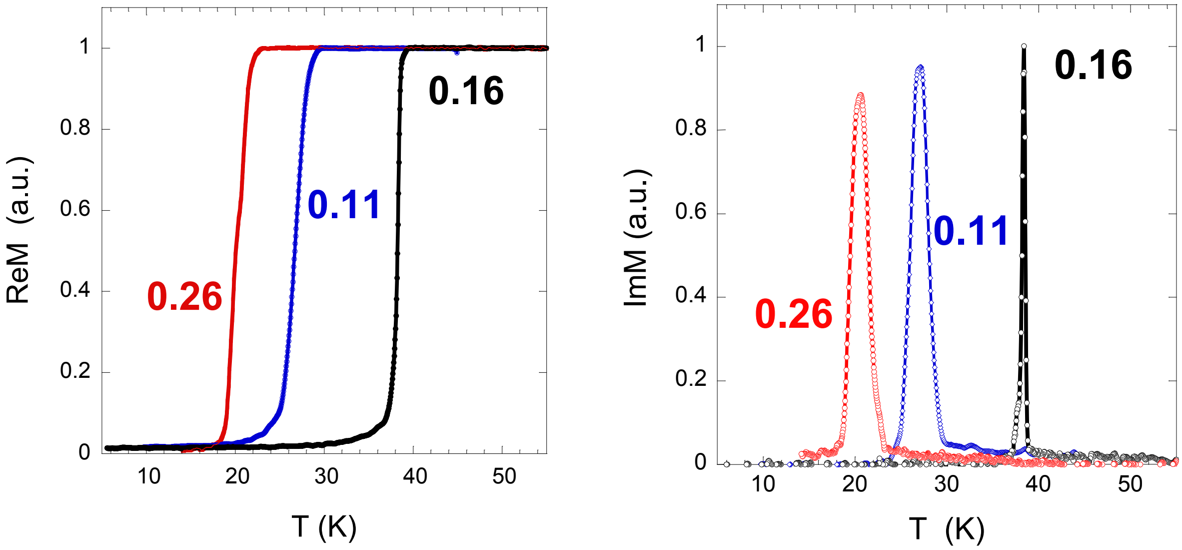

FIG. 7. The real (reactive) part (left panel) and the imaginary (dissipative) part (right panel) of the mutual inductance in three $La_{2-x}Sr_xCuO_4$ films, with the doping level x as indicated. Below T_c a sharp onset of diamagnetic screening is seen in ReM. Sharp peaks in ImM testify to good film homogeneity.

III. FITTING THE RIXS SPECTRA

We fit the spectra reported here using the same approach as Ref. 9: the total spectrum is the sum of three functions, which account for the elastic scattering, the smooth background scattering and the paramagnon respectively. The elastic peak is fit with a Gaussian function of HWHM 130 meV which is a good approximation to the instrumental resolution function. The background from charge transfer excitations and the tail of the dd-excitations is fit with a smooth line. In our case, we used a third-order polynomial, which was multiplied by an exponential factor to make it go smoothly to a constant offset in the negative energy loss region of the spectra. The paramagnon was fit with an antisymmetrized Lorentzian. The scattering intensity $S(\boldsymbol{Q},\omega)$ depends on the imaginary part of the dynamical susceptibility $\chi''(\boldsymbol{Q},\omega)$ and the sample temperature T

$$S(\boldsymbol{Q},\omega) \propto \frac{\chi''(\boldsymbol{Q},\omega)}{1-e^{-\omega/k_B T}}, \tag{1}$$

where k_B is the Boltzmann constant. Due to time reversal symmetry, the dynamical susceptibility must be an odd function of ω, and we model this with an antisymmetrized Lorentzian

$$\chi''(\boldsymbol{Q},\omega) = \frac{\Gamma_{\boldsymbol{Q}}}{(\omega-\omega_{\boldsymbol{Q}})^2+\Gamma_{\boldsymbol{Q}}^2} - \frac{\Gamma_{\boldsymbol{Q}}}{(\omega+\omega_{\boldsymbol{Q}})^2+\Gamma_{\boldsymbol{Q}}^2}. \tag{2}$$

This form for $S(\boldsymbol{Q},\omega)$ was convolved numerically with the Gaussian resolution function.

In line with previous work[9,10], it was not possible to separate the phonon scattering and multi spin flip scattering from the paramagnon. This leads to a slight overestimate (~15%) of the width and intensity of the peak[9]. We note in passing that at the highest doping the magnon becomes extremely broad and fitting the width becomes challenging.

IV. X-RAY ABSORPTION SPECTRA

Given that the RIXS cross section is related (albeit in a complicated way) to the x-ray absorption spectroscopy (XAS) signal[11–13], we present XAS data for the samples here in Fig. 8. At $x = 0$ the Cu L_3 resonance is symmetric in shape. As observed in other studies[14], the main change in the spectra for doped $La_{2-x}Sr_xCuO_4$ is the appearance of a shoulder on the high energy side of the peak. This shoulder is due to the additional states available when holes are doped into the system[14] and it is referred to as the Cu $3d^{10}\underline{L}$ final state where $\underline{L}$ denotes a hole of primarily O $2p$ character. The x-ray energies of interest in our RIXS experiments consist of a window including the Cu L_3 peak extending down in energy to ~500 meV below the L_3 peak, due to the energy loss that occurs in the RIXS process. Within this window, the XAS profiles are similar to within ~20% and this should not change the overall conclusions here. These XAS data was also used to correct for the different film thicknesses used in the experiments.

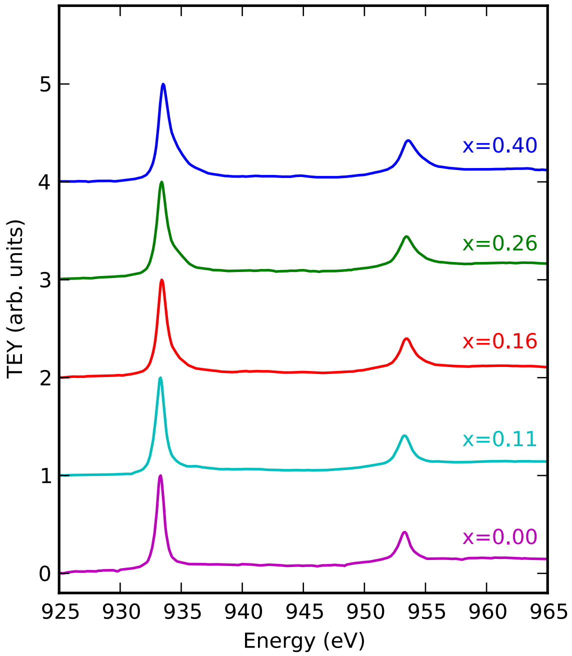

FIG. 8. X-ray absorption spectra measured in total electron yield (TEY) mode. The data were collected with $\theta_i = 30°$ and σ-polarized x-rays. The spectra have been offset from each other for clarity.

V. RIXS INTENSITIES

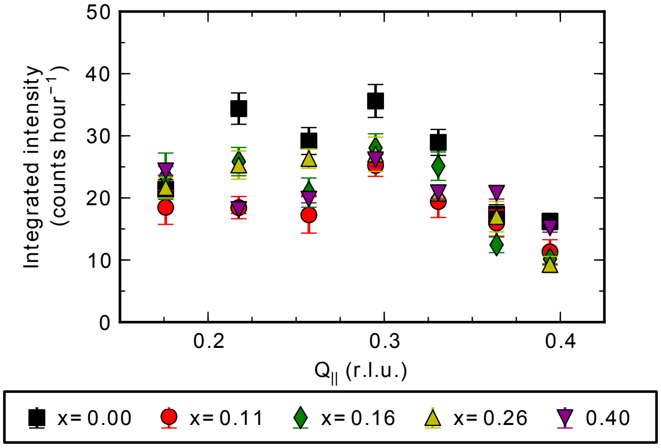

FIG. 9. The intensity of the paramagnon feature in the RIXS data as determined by the fitting procedure. The error bars are the uncertainty in the least square fitting routine. This data was corrected for the different incident x-ray intensity used to measure the $x = 0$ sample. The values at $x = 0.11$ and $x = 0.26$ have been multiplied by 0.78 to account for the fact that they are thicker (see the text for a full explaination).

Figure 9 plots the RIXS intensity of the paramagnon as determined by the fitting procedure. The reduction in intensity at high $\boldsymbol{Q}$ is likely due to increased self absorption as the scattered x-rays have a longer path within the sample. The point-to-point scatter of the data arises primarily from instrumental instabilities: absolute intensity can change due to imperfect alignment and possible drifts in position and energy of incident beam. We estimated the size of this effect by comparing nominally identical spectra taken at different times and this error is included in the error bars in Fig. 3(c) in the main manuscript. We also note here that the $x = 0$ sample was measured with a slightly different experimental configuration (the entrance and exit slits of the beamline monochromator were 20 μm rather than 30 μm). This caused a change in the incident x-ray intensity, which we quantified by measuring the same piece of carbon tape with the two different configurations. The resulting 51% reduction was corrected for in Fig. 3(c) in the main manuscript and Fig. 9 here in the supplementary information. The change in resolution due to this reconfiguration was small, ~ 5%.

In order to compare intensities we also need to correct for the different thicknesses of the films which are either ~ 53 or ~ 99 nm thick. First, we converted the x-ray absorption spectra in Fig. 8 into absolute units. This was done by scaling the pre-edge and post-edge regions of the spectrum to tabulated values of the absorption coefficient, μ,[15,16] and then reading off the relevant value of μ at the Cu L_3 edge. The fraction of x-rays I/I_0 scattered within the film and escaping without being self-absorbed is then

$$\frac{I}{I_0} = \frac{\sin\theta_o}{\sin\theta_i + \sin\theta_o}\left(1 - \exp\left[-t\mu\left(\frac{1}{\sin\theta_i} + \frac{1}{\sin\theta_o}\right)\right]\right) \qquad (3)$$

This equation was evaluated for the scattering angles used to access the $\boldsymbol{Q}$-values measured in Fig. 3(c) in the main manuscript. When averaged over the different $\boldsymbol{Q}$'s, we obtained a factor of 0.78, which was applied to the intensities for the $x = 0.11$ and $x = 0.26$ films in Fig. 9 here and in Fig. 3(c) in the main manuscript. This correction factor is lower than the simple ratio of the thicknesses, due to the fact that the x-rays that scatter from deep within the film are more likely to be self-absorbed before they can escape from the sample. A more sophisticated approach would also consider the polarization dependence[14] of μ. However, the inclusion of these effects would not be expected to change our data by a value larger than the error bars nor would it change the conclusions drawn from the data. Indeed, our conclusions could have been made on the basis of the $x = 0$, $x = 0.16$ and $x = 0.40$ samples, all of which are of the same thickness.

VI. MAGNETIC SPECTRAL INTENSITY

In this section we consider the magnetic spectral intensity in the cuprates. Several studies including Refs. 17 and 18 have shown that spin wave theory provides an acceptable overall description of the magnetic excitations in La_2CuO_4. We recalculated the magnetic dispersions and intensities using the standard spin wave theory expressions provided in Ref. 17 taking the parameters determined via inelastic neutron scattering by Coldea et al. in Ref. 17 with $J = 104$ meV and $J' = -18$ meV describing the first and second nearest neighbor couplings and $Z_c = 1.18$ accounting for the renormalization effects due to quantum fluctuations.[19] We plot the results on the left and central panels of Fig. 10. On the right hand panel of Fig. 10 we mark the regions of the BZ accessible by Cu L_3 edge RIXS in red. We find that 27% of the total inelastic scattering lies within the accessible red region. If we make the assumption that the excitations along $(0,0) \rightarrow (0.4,0)$ and $(0,0) \rightarrow (0.25,0.25)$ scale in a similar way with doping, our results suggest that this 27% of the inelastic magnetic spectral weight in La_2CuO_4 persists as the doping is increased across the $La_{2-x}Sr_xCuO_4$ phase diagram. This is in distinct contrast to the magnetic spectral weight in the blue region centered around $(0.5,0.5)$, which neutron scattering experiments show to be strongly suppressed in intensity and energy.[20–25]

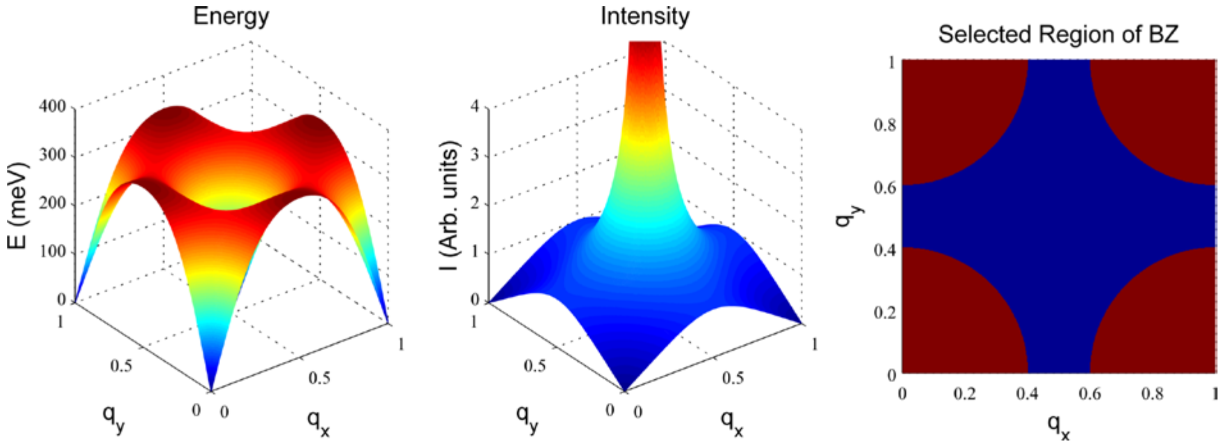

FIG. 10. Calculations based on spin wave theory for the magnetic excitations in La_2CuO_4 showing the evolution of the energy (left panel) and intensity (middle panel) of the magnetic excitations across the Brillouin zone (BZ). The intensity of the excitations diverges at (0.5, 0.5). On the right panel we depict the regions of the BZ assessable by Cu L_3 edge RIXS in red, which consists of a circle of radius 0.4 relative lattice units about $(0,0)$.

---

[1] Božović, I. Atomic-layer engineering of superconducting oxides: yesterday, today, tomorrow. *IEEE Trans. Appl. Supercond.* **11**, 2686 –2695 (2001).

[2] Bollinger, A. T. *et al.* Superconductor-insulator transition in $La_{2-x}Sr_xCuO_4$ at the pair quantum resistance. *Nature* **472**, 458–460 (2011).

[3] Logvenov, G., Gozar, A. & Božović, I. High-temperature superconductivity in a single copper-oxygen plane. *Science* **326**, 699–702 (2009).

[4] Gozar, A. *et al.* High-temperature interface superconductivity between metallic and insulating copper oxides. *Nature* **455**, 782–5 (2008).

[5] Clem, J. R. & Coffey, M. W. Vortex dynamics in a type-II superconducting film and complex linear-response functions. *Phys. Rev. B* **46**, 14662–14674 (1992).

[6] Claassen, J. H., Wilson, M. L., Byers, J. M. & Adrian, S. Optimizing the two-coil mutual inductance measurement of the superconducting penetration depth in thin films. *Journal of Applied Physics* **82**, 3028–3034 (1997).

[7] Turneaure, S. J., Pesetski, A. A. & Lemberger, T. R. Numerical modeling and experimental considerations for a two-coil apparatus to measure the complex conductivity of superconducting films. *Journal of Applied Physics* **83**, 4334–4343 (1998).

[8] Coffey, M. W. Mutual inductance of superconducting thin films. *Journal of Applied Physics* **89**, 5570–5577 (2001).

[9] Le Tacon, M. *et al.* Intense paramagnon excitations in a large family of high-temperature superconductors. *Nature Phys.* **7**, 725–730 (2011).

[10] Dean, M. P. M. *et al.* High-energy magnetic excitations in the cuprate superconductor $Bi_2Sr_2CaCu_2O_{8+\delta}$: Towards a unified description of its electronic and magnetic degrees of freedom. *ArXiv e-prints* (2013). ArXiv:1212.3714 Phys. Rev. Lett. in press.

[11] Ament, L., Ghiringhelli, G., Sala, M., Braicovich, L. & van den Brink, J. Theoretical demonstration of how the dispersion of magnetic excitations in cuprate compounds can be determined using resonant inelastic x-ray scattering. *Phys. Rev. Lett.* **103**, 117003 (2009).

[12] Haverkort, M. W. Theory of resonant inelastic x-ray scattering by collective magnetic excitations. *Phys. Rev. Lett.* **105**, 167404 (2010).

[13] Igarashi, J.-i. & Nagao, T. Magnetic excitations in L-edge resonant inelastic x-ray scattering from one-dimensional cuprates. *Phys. Rev. B* **85**, 064422 (2012).

[14] Chen, C. T. *et al.* Out-of-plane orbital characters of intrinsic and doped holes in $La_{2-x}Sr_xCuO_4$. *Phys. Rev. Lett.* **68**, 2543–2546 (1992).

[15] URL `http://henke.lbl.gov/optical_constants/`.

[16] Henke, B., Gullikson, E. & Davis, J. X-ray interactions: Photoabsorption, scattering, transmission, and reflection at $e = 50 - 30,000$ eV, $z = 1 - 92$. *Atomic Data and Nuclear Data Tables* **54**, 181 – 342 (1993).

[17] Coldea, R. *et al.* Spin waves and electronic interactions in La_2CuO_4. *Phys. Rev. Lett.* **86**, 5377–5380 (2001).

[18] Headings, N. S., Hayden, S. M., Coldea, R. & Perring, T. G. Anomalous high-energy spin excitations in the high-T_c superconductor-parent antiferromagnet La_2CuO_4. *Phys. Rev. Lett.* **105**, 247001 (2010).

[19] Singh, R. Thermodynamic parameters of the T=0, spin-1/2 square-lattice Heisenberg antiferromagnet. *Phys. Rev. B* **39**, 9760–9763 (1989).

[20] Arai, M. *et al.* Incommensurate spin dynamics of underdoped superconductor $YBa_2Cu_3O_{6.7}$. *Phys. Rev. Lett.* **83**, 608–611 (1999).

[21] Bourges, P. *et al.* The spin excitation spectrum in superconducting $YBa_2Cu_3O_{6.85}$. *Science* **288**, 1234–1237 (2000).

[22] Tranquada, J. M. *et al.* Quantum magnetic excitations from stripes in copper oxide superconductors. *Nature* **429**, 534–538 (2004).

[23] Hayden, S. M., Mook, H. A., Dai, P., Perring, T. G. & Dogan, F. The structure of the high-energy spin excitations in a high-transition-temperature superconductor. *Nature* **429**, 531–534 (2004).

[24] Vignolle, B. *et al.* Two energy scales in the spin excitations of the high-temperature superconductor $La_{2-x}Sr_xCuO_4$. *Nature Phys.* **3**, 163–167 (2007).

[25] Xu, G. *et al.* Testing the itinerancy of spin dynamics in superconducting $Bi_2Sr_2CaCu_2O_{8+\delta}$. *Nature Phys.* **5**, 642–646 (2009).